Engineering Journal issn: 0125-8281

Article

Mechanisms of Secondary Flows in a Straight Square Duct under the Effect of Rotation

Wisit Sudjai[1,a], **Varangrat Juntasaro**[1,b], **and Vejapong Juttijudata**[2,c,*]

1 Department of Mechanical Engineering, Faculty of Engineering, Kasetsart University, Bangkhen, Bangkok, 10900, Thailand
2 Department of Aerospace Engineering, Faculty of Engineering, Kasetsart University, Bangkhen, Bangkok, 10900, Thailand
E-mail: [a]wisit.journal@gmail.com, [b]varangrat.j@ku.th, [c,*]vejapong.j@ku.ac.th (Corresponding author)

Abstract. Large eddy simulation with a dynamic kinetic energy subgrid-scale model is employed to simulate three dimensional incompressible fully developed turbulent flows through the non-rotating and rotating straight square ducts at the fixed friction Reynolds number of 300 with various spanwise friction rotation numbers. The study of secondary flows in the duct using the mean streamwise vorticity transport equation is extended up to the friction rotation number of 20. As the duct is rotated, the contribution of streamwise vorticity terms remain the same role for each terms. The reciprocal contributions of streamwise vorticity terms are discovered over the duct cross-sectional area as the duct is rotated. The reciprocal contribution of the convection and rotation terms are found in the upper bottom corner and the lower top corner. On the lateral wall, the diffusion and rotation terms are balanced by each other. The equivalent exchangeable contribution of convection and diffusion terms is also found at upper top corner. The consistent contribution ratio between turbulence to rotation terms is found at reattachment points of small secondary flow cells. Furthermore, the rotational effects tend to drive the turbulent flows to be neutralized into the directional preference along the rotational axis.

Keywords: Large eddy simulation, turbulent flows, streamwise vorticity, rotating duct.

ENGINEERING JOURNAL Volume 28 Issue 5
Received 17 November 2023
Accepted 14 May 2024
Published 31 May 2024
Online at https://engj.org/
DOI:10.4186/ej.2024.28.5.53

DOI:10.4186/ej.2024.28.5.53

1. Introduction

Changes of secondary flows through a rotating and non-rotating ducts appear in many industrial applications. Thus, the straight duct with the square cross-sectional area has regularly been used, over the decades, as the proficient investigation case to reveal the mechanism of the secondary flows.

As an indispensable observation of turbulent flows in the square duct, turbulence induced secondary flows, which naturally occurs in a stationary straight square duct, has been studied by many researchers. The turbulent flows consist of two counter rotating secondary flows distributed in each corner of the duct. Huser and Biringen [1] concluded that the mean shear reduction along the corner bisector allows the mean secondary flows to move toward the duct corners. Therefore, energy is transferred from the duct central region to the corners which results as high velocity zones in the corners [2]. However, not only the energy transfer, but the wall shear stress distribution is also affected by the secondary flows [3]. Furthermore, Vinuesa et al. [4] explained that the secondary flows extract energy from the duct centre to dissipate it at the corner bisector by convect mean velocity from the near-wall region towards the duct core, thus reducing the wall shear stress. However, Speziale [5] proved that the secondary flows will occur when nonzero normal Reynolds stress difference on planes perpendicular to the axial flow direction take place due to the axial mean velocity. Although, the turbulent normal stresses anisotropy does not play a major role in the secondary flow generation, but primarily the Reynolds shear stress gradients does the role in the corner region [6].

Despite the secondary flows of turbulent motion, the secondary flows in the stationary duct can be altered by effects of rotation. The Coriolis force, which is induced by the spanwise rotation, causes several changes to the secondary flows. For instance, turbulent flows in the rotating duct is divided into unstable side, where the turbulent flows was made unstable, and stable side, where the turbulent flows was made stable [7-11]. Moreover, the turbulence induced secondary flows is converted into the Coriolis driven secondary flows, which consists of two large counter rotating secondary flows and two small secondary flows on the unstable wall. The secondary flows pattern in the rotating duct was observed by Dai et al. [10] and concluded that the additional vortices are grown and released with various position of separation point but fixed reattachment point near the corners on the unstable wall. Therefore, wall shear stress distribution is influenced by the secondary flows [10, 11], and thus, boundary layers and flow structures would be impacted as a consequence [11]. As the rotation number increases, thin boundary layers, which is Ekman layers, are formed on the lateral walls. The boundary layers normally cause a high contribution to the most pressure drop of the flows [9]. Apparently, Taylor-Proudman region is placed in the central region of

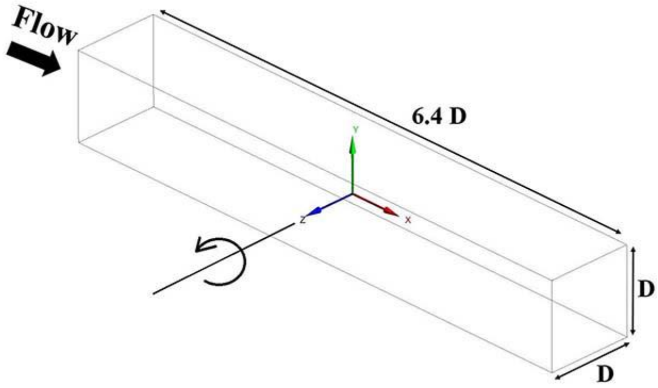

Fig. 1. Computational domain.

the rotating duct, which indicates the constant streamwise velocity along the axis of rotation. Therefore, the rotation effects tend to stabilize the turbulent flows to be the Taylor-Proudman regimes which yields the zero streamwise vorticity in the rotating duct central region [7]. Thus, rotation tend to stabilize the turbulent flows on the stable side and the lateral walls as the rotation number increases [7, 10, 11]. Moreover, turbulent kinetic energy and transport of Reynolds stresses are dominated by the Coriolis force due to the system of rotation [11].

In contrast with the turbulent motion which generates the secondary flows in the non-rotating duct, the other secondary flows appear in the rotating duct tend to be dominated by the Coriolis effects. Therefore, investigation into the variety of mechanism changes of the secondary flows through the straight square duct under the effects of rotation is the aim of this paper. Although, researchers have investigated the secondary flows with the friction rotation number up to 50 using the mean momentum budget, Reynolds stress budget, and pre-multiplied energy spectra but none of researchers have evaluated the secondary flows using the mean streamwise vorticity transport equation with high friction rotation number up to 20 [7, 8, 10-12]. Thus, this paper extend the study further from Pallares and Davidson [7] to the higher friction rotation number. The incompressible fully developed turbulent flows through the stationary and rotating straight square ducts at fixed friction Reynolds number of 300 with various friction rotation numbers of 0, 1.3, 5, 10, and 20 are investigated. The study of the stationary case is considered as the baseline of the changes. Meanwhile, the others are chosen since they expose the significant flow patterns. For instance, the second and the last considered friction rotation numbers demonstrate almost two large secondary flows, while the third and the fourth display two large secondary flows with visible two small secondary flows on the unstable wall [10].

The general statistics of those secondary flows are described through mean velocity and turbulence statistics in section 3. Furthermore, the mean streamwise vorticity transport equation terms are accessed to expose the secondary flows in section 4.

Table 1. The bulk Reynolds numbers and the bulk rotation numbers comparison between the present results and the reference data at the fixed friction Reynolds number of 300 with various friction rotation numbers of 0, 1.3, 5, 10, and 20.

	Present work		**Dai et al. (2015)**		**Pallares et al. (2005)**		**Gavrilakis (1992)**	
Ro_τ	Re_b	Ro_b	Re_b	Ro_b	Re_b	Ro_b	Re_b	Ro_b
0	4462.4	0	4418	0	-	-	4410	0
1.3	3947.3	0.0987	3924	0.099	-	-	-	-
5	3112.4	0.4819	3124	0.480	3080	0.49	-	-
10	2684.1	1.1176	2708	1.108	2650	1.13	-	-
20	2299.6	2.6090	2297	2.612	2250	2.66	-	-

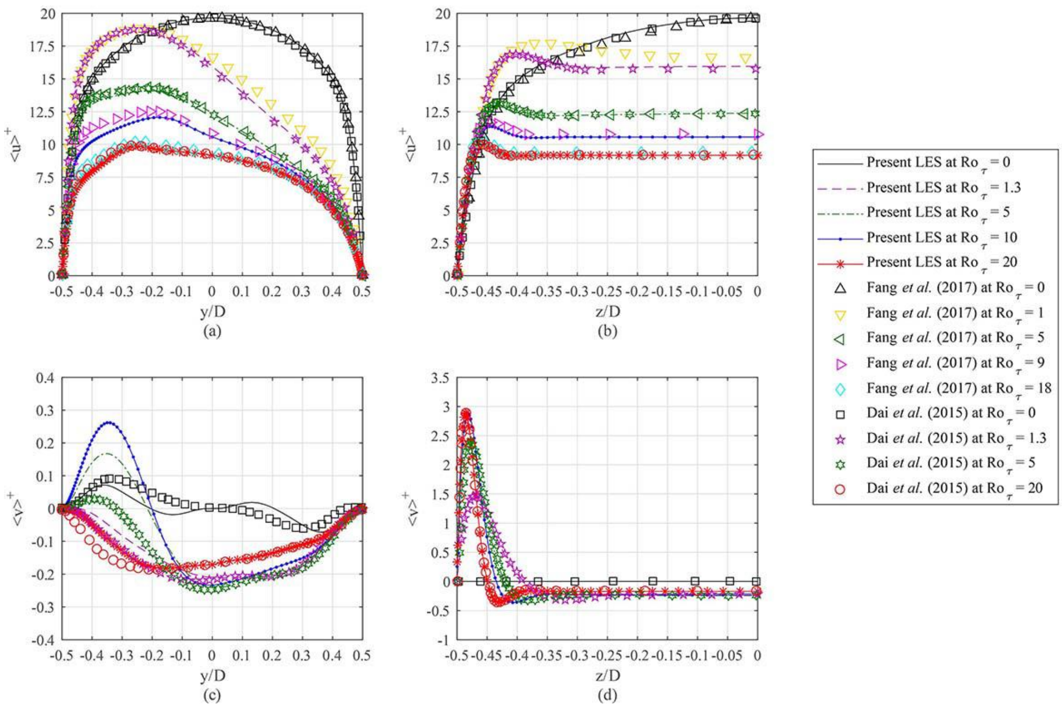

Fig. 2. The dimensionless mean streamwise velocity profiles (upper row) and the dimensionless mean normal velocity profiles (lower row) at the different friction rotation numbers along the wall bisectors at (a), (c) z/D = 0; and (b), (d) y/D = 0.

2. Methodology

2.1. Computational Domain and Boundary Conditions

The incompressible fully developed turbulent flows in the non-rotating and rotating straight square ducts are simulated in the computational domain, as shown in Fig. 1. The cross-sectional area of the fluid domain has a size of D x D, where D denotes the duct hydraulic diameter. Furthermore, the domain is extended in the streamwise direction with length of 6.4D. The coordinate origin is located at the middle of the duct. Moreover, the x, y, and z coordinates are represented as the streamwise, normal, and spanwise directions, respectively. Therefore, the velocity components in x, y, and z axis are denoted as u, v, and w velocity components, respectively. Lastly, the spanwise direction rotation axis is placed at the center of the computational domain.

In this paper, ANSYS Meshing is conducted to generate the suitable computational mesh in order to expose the mechanism of turbulent flows in the ducts under the effects of rotation. Hexahedral mesh is built by using the Multizone method. The mesh is uniformly divided into 81 grid points along the streamwise direction, using the edge sizing method, in order to efficiently capture the streamwise streak turbulence structures. Likewise, the edge sizing method is also used to arrange the mesh over the duct cross-sectional area. For each edge along the perimeter of the cross-sectional area, the 109 grid points with smooth transition bias growth rate of 1.06 is chosen. Thus, the corresponding grid spaces are the uniform grid spacing of $(\Delta x^+) = 24$ and the grid spaces of $(\Delta y^+)_{min} = (\Delta z^+)_{min} = 0.4$ and $(\Delta y^+)_{max} = (\Delta z^+)_{max} = 8.77548$ over the cross-sectional

DOI:10.4186/ej.2024.28.5.53

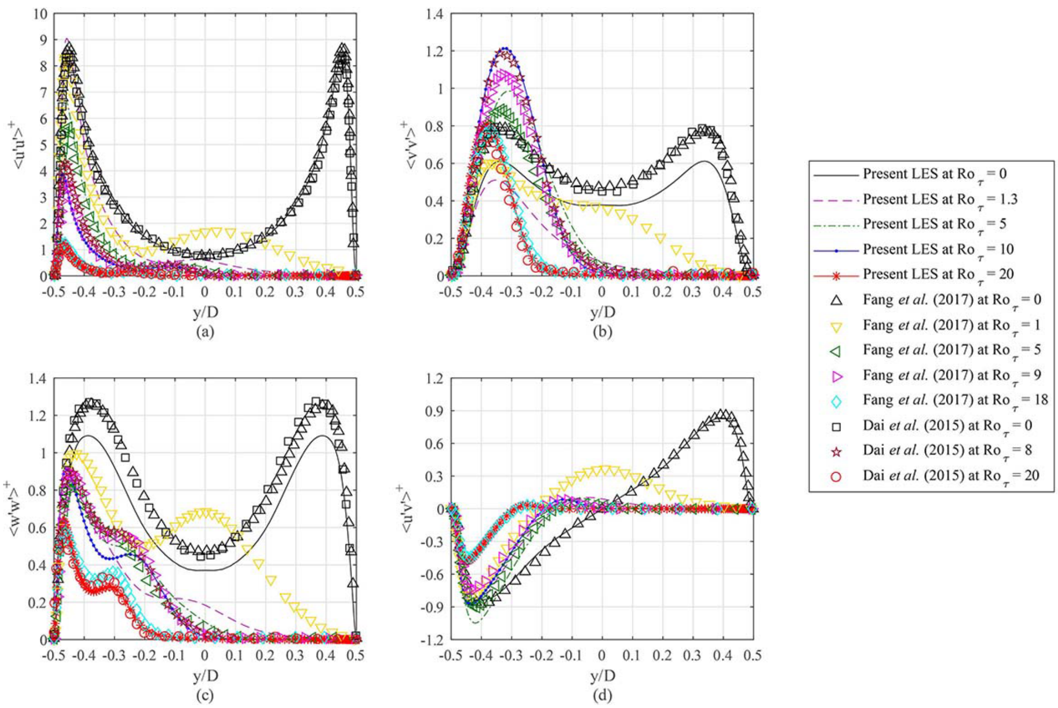

Fig. 3. The dimensionless turbulence intensity profiles, (a) $\langle u'u' \rangle^+$; (b) $\langle v'v' \rangle^+$; (c) $\langle w'w' \rangle^+$; and (d) $\langle u'v' \rangle^+$, at different friction rotation numbers along the wall bisector at z/D = 0.

area. Consequently, the 81 x 109 x 109 grid points with the 1.06 bias growth rate computational mesh is generated.

Meanwhile, the non-slip boundary condition is imposed on each wall of the duct. The rotating reference frame is enabled with the relative velocity formulation in order to adjust the friction rotation number. Moreover, the translational periodic condition is authorized by setting the streamwise pressure gradient equals to -4 to take on the fully developed flows and keep the friction Reynolds number to be constant. In addition, the friction Reynolds number is defined as $Re_\tau = u_\tau D/\nu$ and the friction rotation number is defined as $Ro_\tau = 2\Omega D/u_\tau$ where u_τ is the friction velocity, ν is the kinematic viscosity, and Ω is the angular velocity of system rotation. Thus, the fixed friction Reynolds number of 300 with the friction rotation numbers of 0, 1.3, 5, 10, and 20 cases are considered.

2.2. Numerical Simulation

The filtering incompressible Navier-Stokes equations are employed by using the ANSYS Fluent 18.1 CFD software. In addition, the universal isotropic small eddies, which have sizes smaller than the filter width or grid spacing, are filtered out by applying the filtering operation. Thus, the most energetic large eddies, in the energy containing range and also in the inertial subrange, are left in the equations as the resolved flow field. However, the unresolved small eddies in subgrid scale stress tensor are needed to be modeled.

Large Eddy Simulation (LES) with a dynamic kinetic energy subgrid scale model proposed by Kim and Menon [13] is performed, detail of the subgrid scale model is shown in Kim [14]. This turbulent kinetic energy subgrid scale transport model allows for the history, non-equilibrium effects to be taken into account [14]. Several studies of the dynamic LES model in various kind of flows confirmed that the dynamic kinetic energy subgrid scale model has the potential to predict complex flows [13-17]. Moreover, the model has been successfully implemented by many researchers to simulate the turbulent flows in a straight square duct at various rotation numbers [7, 8, 18].

The subgrid scale kinetic energy transport equation is expressed as

$$\varrho \frac{\partial k_{sgs}}{\partial t} + \varrho \frac{\partial \bar{u}_j k_{sgs}}{\partial x_j} = -\tau_{ij}\frac{\partial \bar{u}_i}{\partial x_j} - C_\varepsilon \varrho \frac{k_{sgs}^{3/2}}{\Delta_f} + \frac{\partial}{\partial x_j}\left(\frac{\mu_t}{\sigma_k}\frac{\partial k_{sgs}}{\partial x_j}\right) \quad (1)$$

where ϱ is the density, $\bar{u}_i$ is the resolved velocity field, τ_{ij} is the subgrid-scale stress, C_ε is the dynamically determined coefficient, Δ_f is the filter width, and σ_k equals to 1.

By solving the transport equation in Eq. (1), the subgrid scale kinetic energy, k_{sgs}, is obtained as

$$k_{sgs} = \frac{1}{2}\left(\overline{u_k^2} - \bar{u}_k^2\right) \quad (2)$$

Thus, the subgrid scale eddy viscosity, μ_t, is achieved by substituting the k_{sgs} as

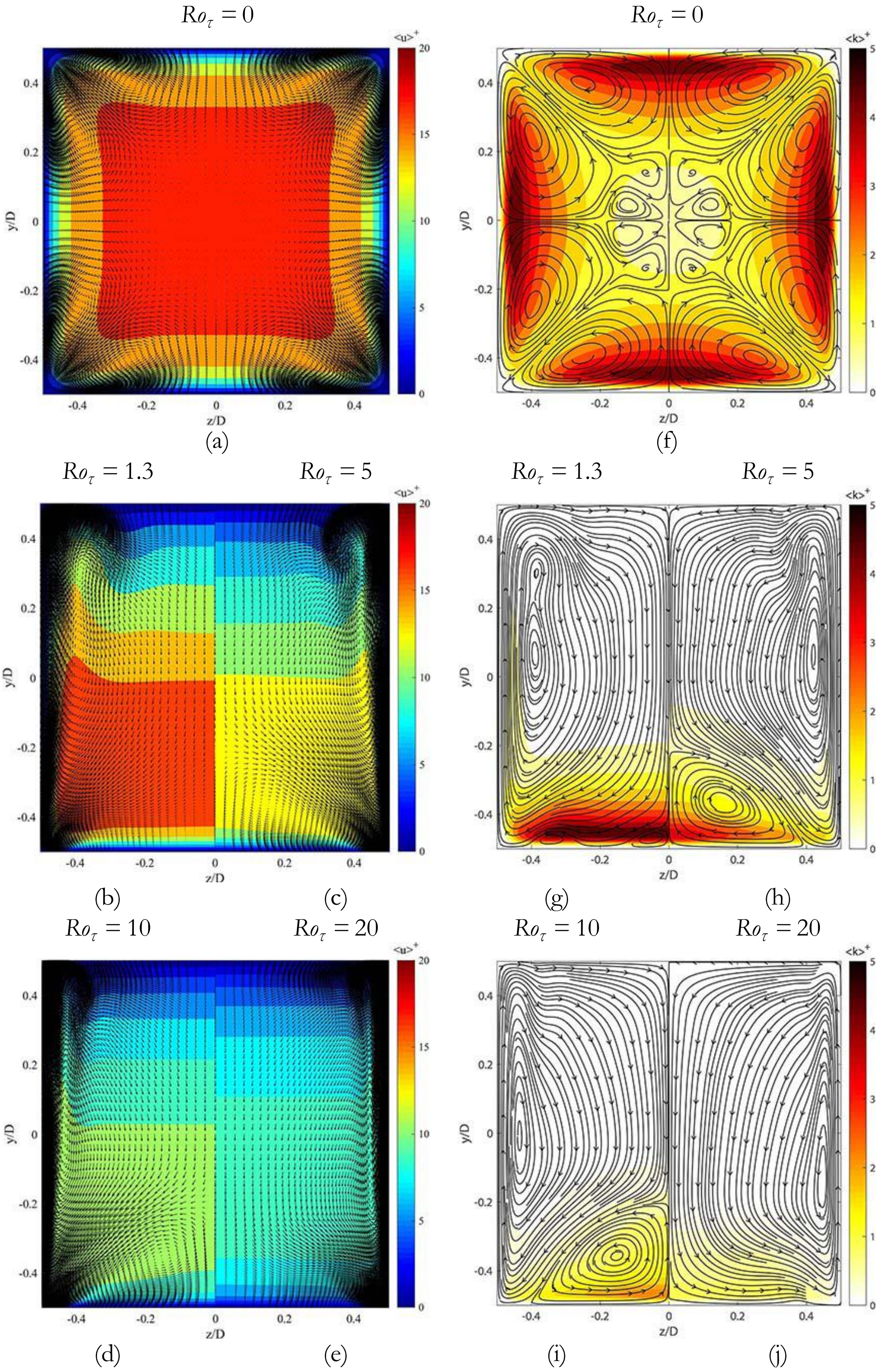

Fig. 4. The dimensionless mean streamwise velocity contours overlaid with the dimensionless mean cross-sectional velocity vectors (left column) and the dimensionless mean turbulent kinetic energy contours overlaid with the dimensionless cross-sectional velocity streamlines (right column) at different friction rotation numbers.

$$\mu_t = C_k \varrho k_{sgs}^{1/2} \Delta_f \quad (3)$$

where C_k is the dynamically determined coefficient.

Accordingly, the subgrid scale stress tensor, τ_{ij}, is modelled as follows:

$$\tau_{ij} - \frac{2}{3}\varrho k_{sgs}\delta_{ij} = -2C_k \varrho k_{sgs}^{1/2} \Delta_f \bar{S}_{ij} \quad (4)$$

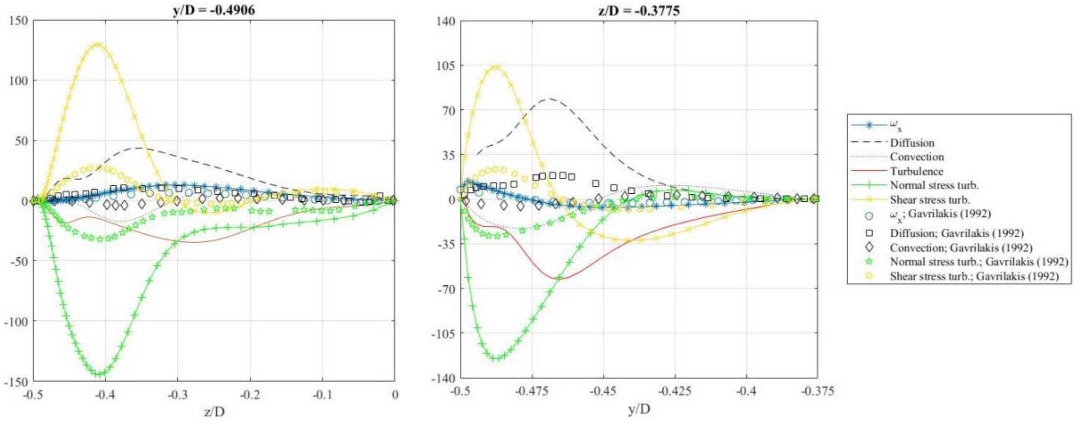

Fig. 5. The resolved ω_x and its transportation terms at $Ro_\tau = 0$ (a) along the spanwise direction at y/D = -0.4906, and (b) along the normal direction at z/D = -0.3775.

where δ_{ij} is the Kronecker delta.

The rate of strain tensor for the resolved field is defined as

$$\bar{S}_{ij} \equiv \frac{1}{2}\left(\frac{\partial \bar{u}_i}{\partial x_j} + \frac{\partial \bar{u}_j}{\partial x_i}\right) \quad (5)$$

The present Large Eddy Simulation (LES) of the three-dimensional incompressible fully developed turbulent flows in the straight square duct at various friction rotation numbers is done by using the precursor RANS (Reynolds-Averaged Navier-Stokes) solutions with the superimposed synthetic turbulence on its mean flow field as the initial condition for each LES case.

The pressure-based solver is used with the fractional step method as the pressure-velocity coupling scheme. The least-squares cell based is used for the gradient interpolation scheme. The second-order scheme is applied for the pressure and the central differencing method for momentum and subgrid kinetic energy equations. For transient formulation scheme, the second order implicit is used. Lastly, the non-iterative time advancement is also employed. However, for the case of the friction rotation number at 20, the bounded central differencing method is used for the momentum and subgrid kinetic energy equations in the spatial discretization scheme to avoid the unphysical oscillation as suggested in ANSYS, Inc. [16]. The time step size is chosen to keep the maximum CFL number to be below 1. The sampling procedure is conducted after the sampling period of $600D/u_\tau$ for each case. In addition, the sampling rate is not collected over $0.1D/u_\tau$. For post-processing of the calculated results, the results are averaged along the streamwise direction. For the stationary case, the quadrant average is done, by average two opposite sides along y axis and consequently average other two opposite side along x axis, for mean velocity field and turbulence statistics. However, the octant average is conducted, by do the quadrant average and average the results again along diagonal line of the duct, for the mean streamwise vorticity transport equation terms for the stationary case. Furthermore, two opposite sides along the y axis are averaged together for the rotating cases, due to the symmetry of the flows.

3. Mean Velocity and Turbulence Statistics

3.1. Validation of Mean Velocity and Turbulence Statistics

To clearly manifest the mechanism of square duct secondary flows in following sections, mean velocity and turbulence statistics profiles are validated in this subsection 3.1, by comparing the present results with existing reference results.

In this subsection, the general statistics of the incompressible fully developed turbulent flows in the non-rotating and rotating straight square ducts are validated against the previous authors' results published in the past. In addition, the mean flow field and the turbulence intensities are normalized by the friction velocity, u_τ. The distance in the x, y, and z directions are normalized by the hydraulic diameter, D.

As illustrated in Table 1, the present results of the Reynolds numbers and the rotation numbers based on the bulk velocity, U_b, and the hydraulic diameter are compared with the existing data at the different rotation numbers. The results show the significant decreasing trend of the bulk Reynolds numbers consistent with the references, as the rotation number increases. Moreover, the overall percentage difference between the present work and the references is about 2 percent.

The dimensionless mean velocity profiles along the y and z axis and the dimensionless turbulence intensity profiles along the y axis at the different friction rotation numbers are shown in Fig. 2 and 3, respectively. Although, the discrepancy is observed in Fig. 2 and 3 but the results agree qualitatively well with the references [10, 11] and many authors using the LES [18-21]. The dimensionless mean streamwise velocity profiles, $\langle u\rangle^+$,

DOI:10.4186/ej.2024.28.5.53

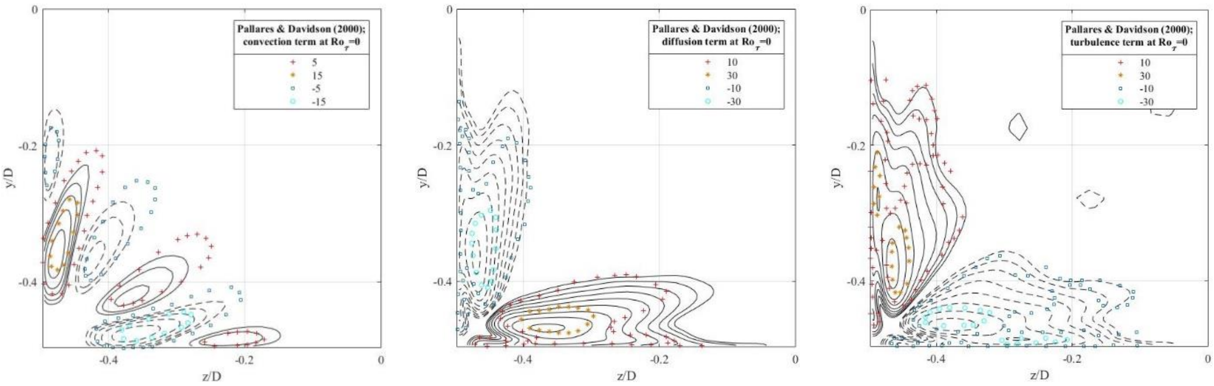

(a) (b) (c)

Fig. 6. The resolved ω_x transportation terms at $Ro_\tau = 0$; (a) convection term; (b) diffusion term; (c) turbulence term. Solid and dash lines for positive and negative values, respectively. The values of the contour lines are the minimum values of -5 and 5 with the 1.4 multiplication decrement and increment, respectively, in every step of the intervals (e.g. ..., -7, -5, 0, 5, 7, ...).

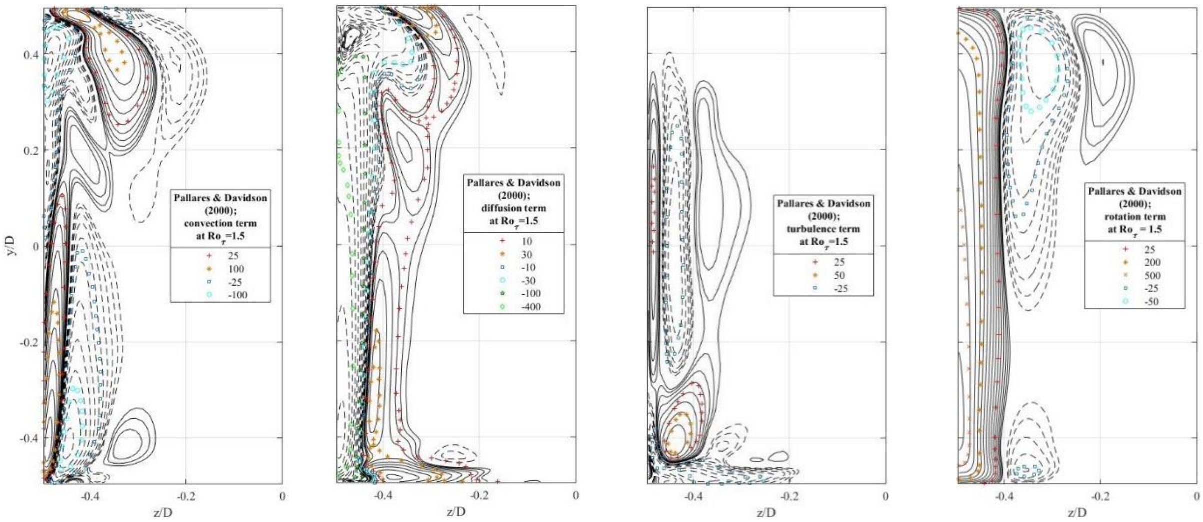

(a) (b) (c) (d)

Fig. 7. The resolved ω_x transportation terms at $Ro_\tau = 1.3$; (a) convection term; (b) diffusion term; (c) turbulence term; (d) rotation term. Solid and dash lines for positive and negative values, respectively. The values of the contour lines are the minimum values of -5 and 5 with the 1.4 multiplication decrement and increment, respectively, in every step of the intervals (e.g. ..., -7, -5, 0, 5, 7, ...).

along the wall bisectors, show the magnitude reduction due to the rotational effects, as shown in Fig. 2(a) and 2(b), corresponding with the results mentioned in Table 1. Meanwhile, the turbulent flows tend to be confined at the bottom wall. The Taylor-Proudman region, where the dimensionless mean streamwise velocity is constant along the rotational axis, is observed in the central region of the duct and continuously expands in the spanwise direction as the rotation number increases, as shown in Fig. 2(b). In Fig. 2(d), the dimensionless mean vertical velocity profiles, $\langle v\rangle^+$, are amplified and pressed on the lateral walls which result as the thin boundary layers, Ekman layers, on the walls as the rotation number increases. In Fig. 2(c), as the rotation number increases, the appearance of additional vortices are observed on the bottom wall, corresponding with the references.

Figure 3 shows the dimensionless turbulence intensity profiles along the y axis at various friction rotation numbers. The present results are consistent with the references. The turbulent flows can be distinguished into two sides, as shown in Fig. 3. One is the unstable side on the bottom wall, and another one is the stable side on the top wall. Although, the turbulence is forced to be restricted at the unstable side, the overall turbulence intensity is reduced, as the rotation number increases, corresponds with the previous discussion in Table 1.

3.2. Flow Patterns and Turbulent Kinetic Energy Distribution

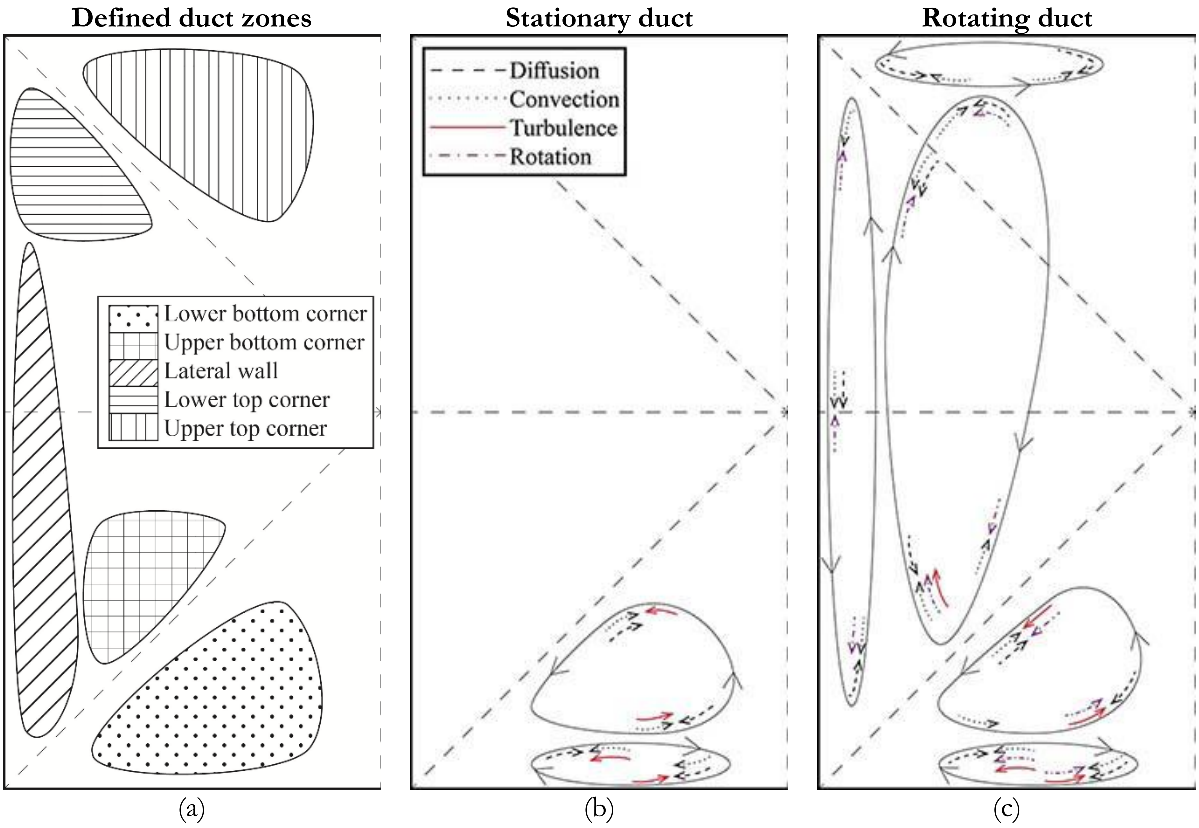

Fig. 8. (a) defined duct zones; the schematic mechanisms of the resolved ω_x transportation terms of (b) stationary duct and (c) rotating duct. Sketch of secondary flows represent the resolved ω_x. Arrow directions represent the contribution of each resolved ω_x transportation terms (e.g. arrow direction follows the resolved ω_x means the resolved ω_x transportation terms have the same plus or minus signs as the resolved ω_x and arrow direction encounters the resolved ω_x means the resolved ω_x transportation terms have the opposite plus or minus signs to the resolved ω_x).

In this subsection, nature of mean secondary flow cells under the effect of rotation is displayed in Fig. 4 using the contour of dimensionless mean streamwise velocity overlaid with the dimensionless mean cross-sectional velocity vectors, Fig. 4(a) to 4(e), and the contour of dimensionless mean turbulent kinetic energy overlaid with the streamlines of dimensionless mean cross-sectional velocities, Fig. 4(f) to 4(j). Only half of the duct is shown due to the symmetry of the flows, the Fig. 4(b) to 4(e) and the Fig. 4(g) to 4(j).

The present results show that the flow patterns and the turbulent kinetic energy distribution are consistent with the other researchers [1-4, 6-12, 18-21].

Without rotation, there are eight secondary flow cells in the duct cross-sectional area which consist of the two counter-rotating secondary flows symmetrically distributed along the corner bisectors. As the rotation number increases, the rotation effects alter the secondary flows which appear in the stationary duct to be the two large secondary flow cells with the growth and diminishment of the other two small secondary flow cells on the bottom wall. Moreover, as shown in Fig. 4, the reattachment points are fixed at the bottom corners while the separation points are varied above the unstable wall as the rotation number increases, coincident with observation of Dai et al. [10]. The Taylor-Proudman region is evidently noticed in the central region of the rotating duct where the dimensionless mean streamwise velocity is constant, as shown in Fig. 4(b) to 4(e). Moreover, the dimensionless mean streamwise velocity is decreased as the rotation number increases due to the Coriolis force in accordance with Table 1 and Fig. 2. However, as shown in Fig. 4(b) to 4(e), the Ekman layers are placed on the lateral walls.

As shown in Fig. 4(g) to 4(j), the dimensionless turbulent kinetic energy is confined on the unstable side while the energy is suppressed in the central region, where the Taylor-Proudman region is located, and on the lateral walls, where the Ekman layers are placed, as the rotation number increases.

4. Mean Streamwise Vorticity

The transport equation of resolved mean streamwise vorticity, $\omega_x = \partial\langle w\rangle/\partial y - \partial\langle v\rangle/\partial z$, is used to disclose the flow mechanism of the incompressible fully developed turbulent flows in the straight square duct under the effect of rotation at various friction rotation numbers.

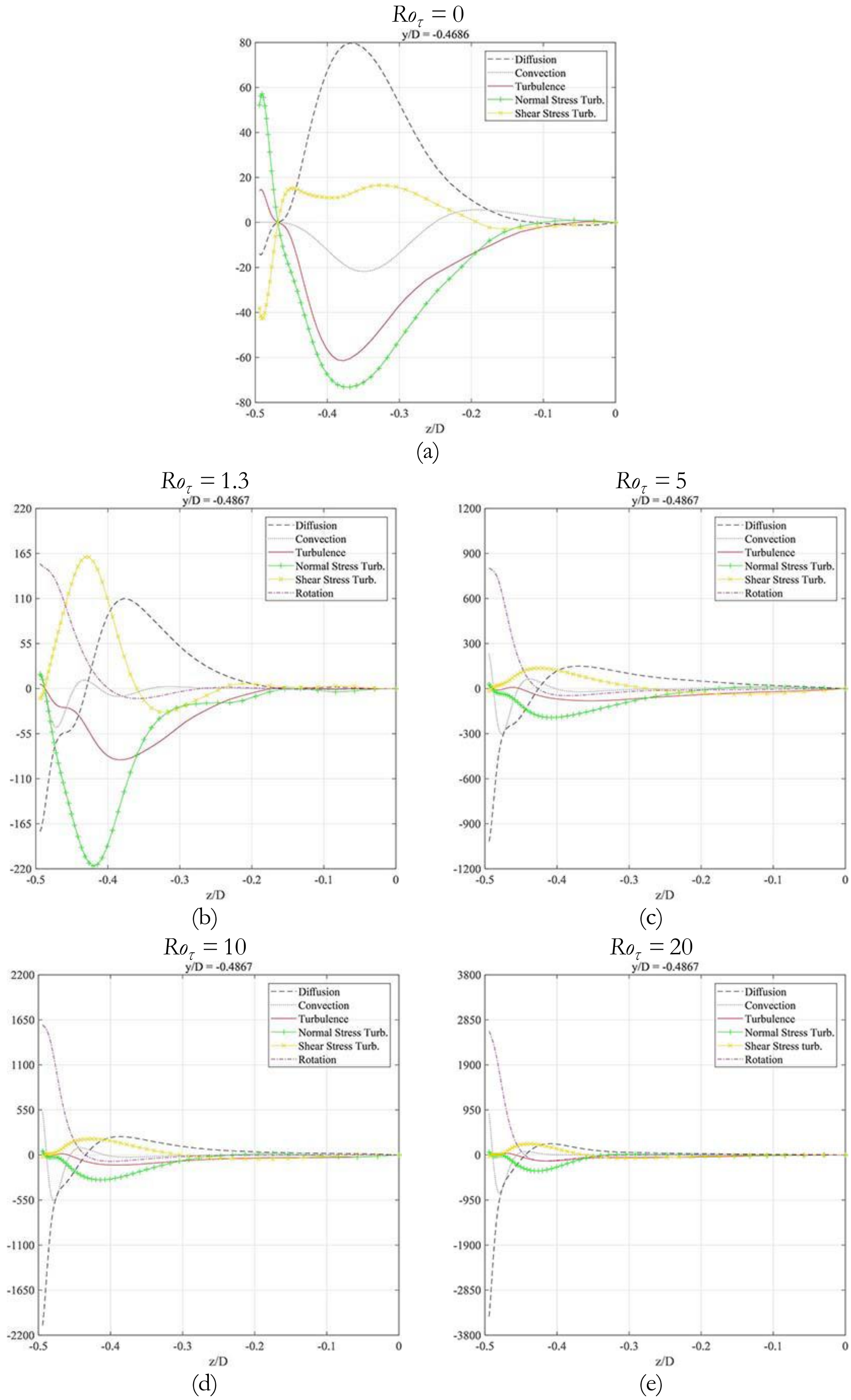

Fig. 9. The resolved ω_x transportation terms at the lower bottom corner (a) $Ro_\tau = 0$; (b) $Ro_\tau = 1.3$; (c) $Ro_\tau = 5$; (d) $Ro_\tau = 10$; (e) $Ro_\tau = 20$.

DOI:10.4186/ej.2024.28.5.53

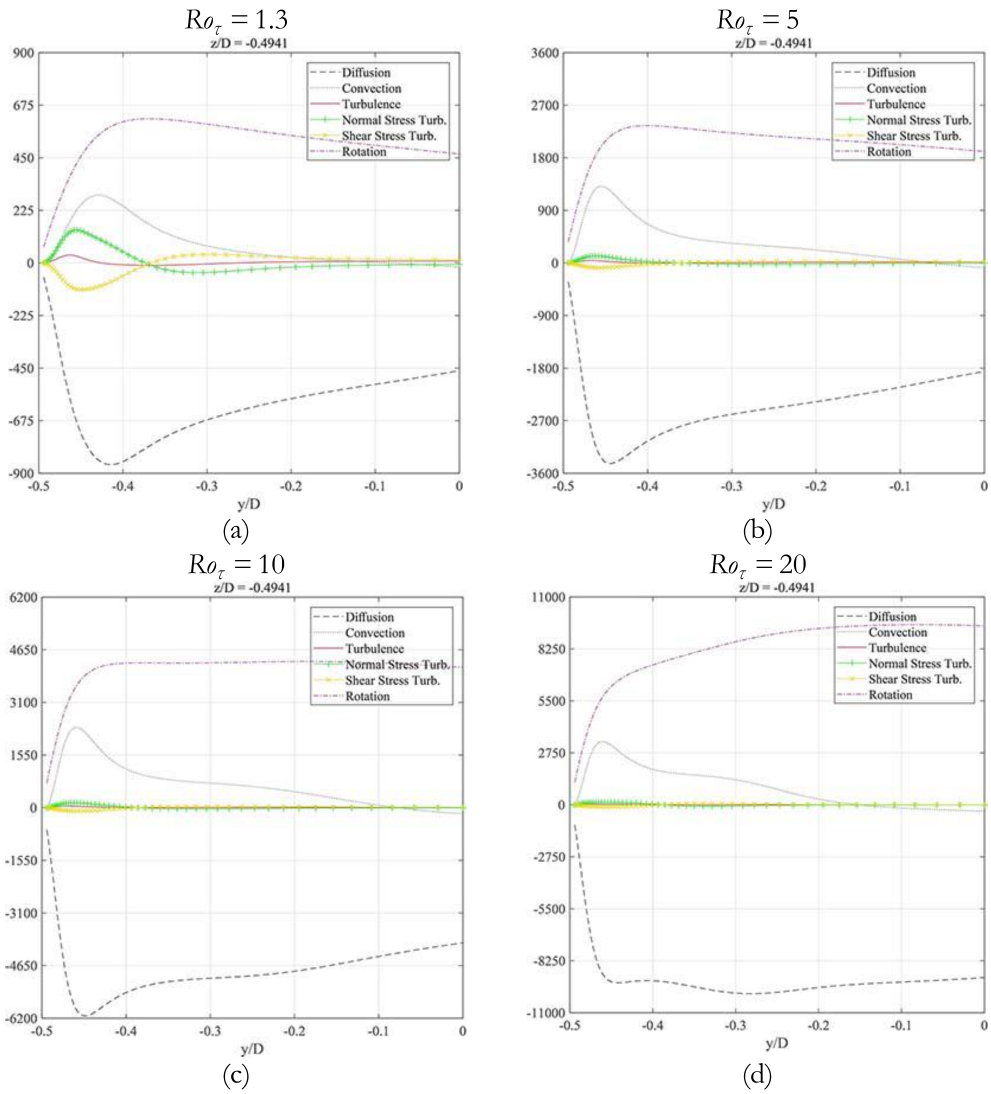

Fig. 10. The resolved ω_x transportation terms at the lateral wall (a) $Ro_\tau = 1.3$; (b) $Ro_\tau = 5$; (c) $Ro_\tau = 10$; (d) $Ro_\tau = 20$.

The equation is expressed as

$$\left(\frac{\partial}{\partial z}\left(\left(\frac{1}{Re_\tau} + \langle \nu_T \rangle\right)\frac{\partial}{\partial z}\right) + \frac{\partial}{\partial y}\left(\left(\frac{1}{Re_\tau} + \langle \nu_T \rangle\right)\frac{\partial}{\partial y}\right)\right)\omega_x$$
$$- \left(\langle v \rangle \frac{\partial}{\partial y} + \langle w \rangle \frac{\partial}{\partial z}\right)\omega_x$$
$$+ \left(\frac{\partial^2}{\partial y \partial z}\left(\langle v'^2 \rangle - \langle w'^2 \rangle\right)\right) + \left(\frac{\partial^2}{\partial z^2} - \frac{\partial^2}{\partial y^2}\right)\langle v'w' \rangle$$
$$+ Ro_\tau \frac{\partial \langle u \rangle}{\partial z} + SGS_{\omega_x} = 0 \qquad (6)$$

There are six terms in Eq. (6). The first term is the diffusion term. The second term is the convection term. However, the third term, which is the normal stress turbulence term, and the fourth term, which is the shear stress turbulence term, are summed together to be represented as the turbulence term. The fifth term is the rotation term. Lastly, the sixth term, the subgrid scale term, is negligible since this term has small influence to the transport equation which corresponds to the discussion in Pallares and Davidson [7].

4.1. Mean Streamwise Vorticity Validation

Firstly, in this subsection, the present results are validated against DNS data of Gavrilakis [3] and LES data of Pallares and Davidson [7], to ensure the correctness of the resolved ω_x transportation terms. For stationary duct, the DNS [3] and the LES [7] data are used as references at $Ro_\tau = 0$. However, for rotating duct, the LES [7] data at the friction rotation number of 1.5 is used as reference for the present LES results at $Ro_\tau = 1.3$.

As shown in Fig. 5(a) and Fig. 5(b), the resolved ω_x results are in-line with the DNS data [3]. Although, each term in the resolved ω_x transport equation has difference values with the reference [3] but the present LES gives results in the same direction consistent with the reference of DNS data [3]. Furthermore, contours of the resolved ω_x transportation terms are plotted for the stationary and rotating ducts validation as shown in Fig. 6 and Fig. 7,

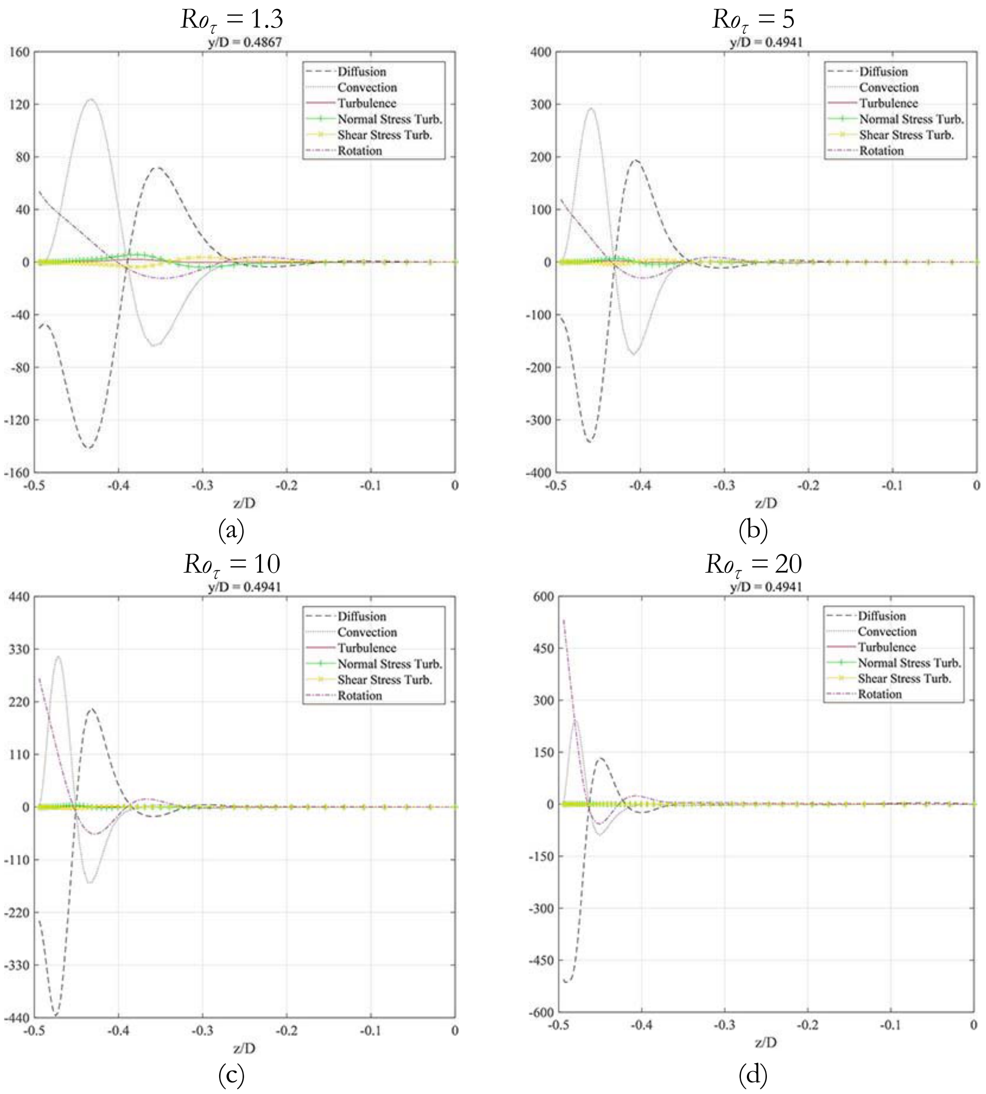

Fig. 11. The resolved ω_x transportation terms at the upper top corner (a) $Ro_\tau = 1.3$; (b) $Ro_\tau = 5$; (c) $Ro_\tau = 10$; (d) $Ro_\tau = 20$.

respectively. As shown in both Fig. 6 and Fig. 7, the present LES results and the reference LES data [7] display the same configuration for the resolved ω_x transportation terms distribution. In addition, since subgrid-scale model have to rely on the grid size to model small eddies [16], it is a nature of LES to obtain the discrepancies between the present LES results and the references [3, 7] due to different computational grids, which were implemented in each work.

4.2. Straight Square Duct Secondary Flows' Mechanisms

Foremost, stationary duct is investigated as a baseline mechanism of the secondary flows under rotation effects in subsubsection 4.2.1. Consequently, rotating duct is mentioned in following subsubsection 4.2.2. To identify secondary flows produced in a square duct under rotation effect, five zones are defined over the duct cross section as lower bottom corner, upper bottom corner, lateral wall, lower top corner, and upper top corner, as shown in Fig. 8(a).

Highlighted dominant streamwise vorticity terms balance of each eddies are evaluated and summarized in sketches of secondary flows as shown in Fig. 8(b) and 8(c). The resolved ω_x is enlarged and represented as the secondary flows in the sketches which established by the right hand rule. Inward and outward sketched secondary flows represent the positive and negative streamwise vorticity, respectively. In addition, the resolved ω_x transportation terms' arrow direction follows the sketched resolved ω_x means the resolved ω_x transportation terms have the same plus or minus signs as the resolved ω_x . However, the resolved ω_x transportation terms' arrow direction encounters the sketched resolved ω_x means the resolved ω_x transportation terms have the opposite plus or minus signs to the resolved ω_x.

As shown in Fig. 8(b) and 8(c), the resolved ω_x transportation term balances are highlighted in every

DOI:10.4186/ej.2024.28.5.53

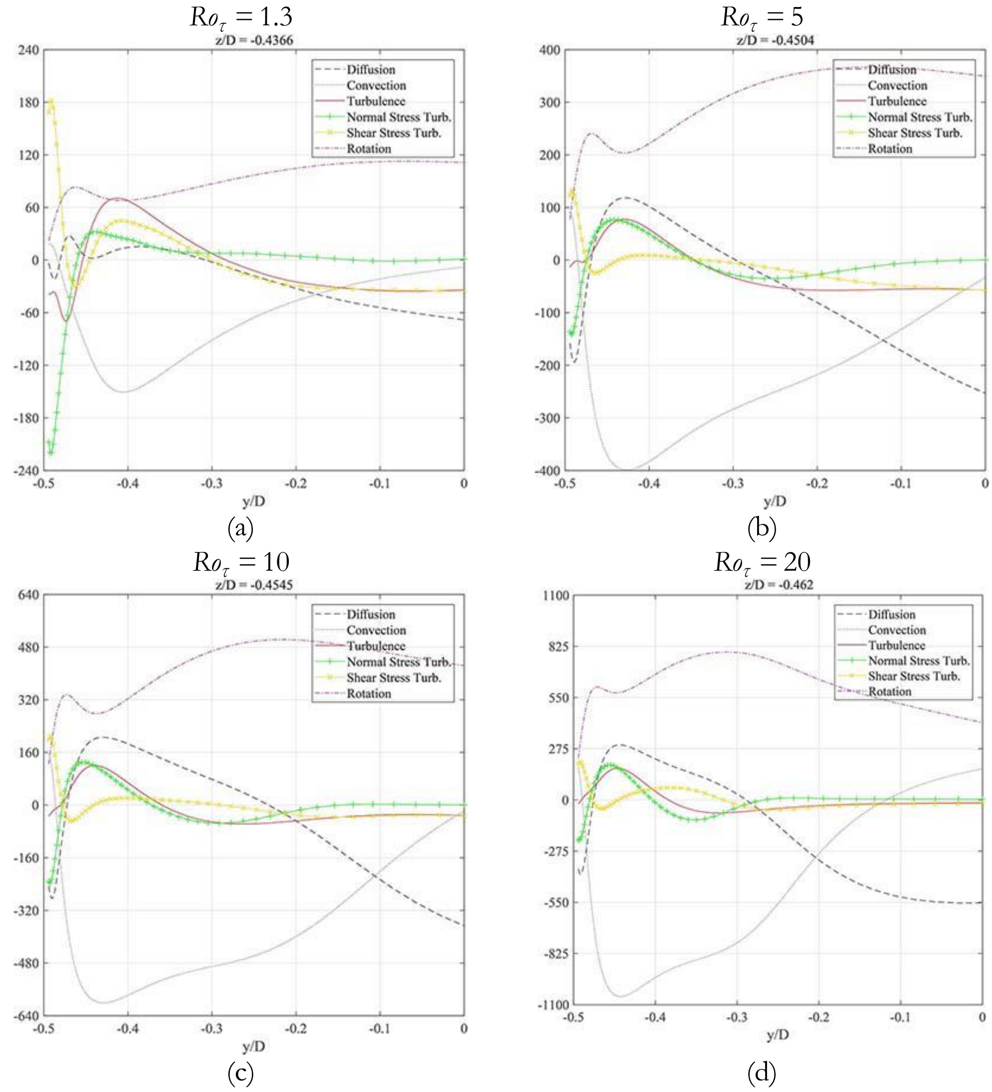

Fig. 12. The resolved ω_x transportation terms at the upper bottom corner (a) $Ro_\tau = 1.3$; (b) $Ro_\tau = 5$; (c) $Ro_\tau = 10$; (d) $Ro_\tau = 20$.

zones in the duct cross sectional area. Four locations are highlighted for both stationary and rotating ducts in the lower bottom corner. For rotating duct, two locations are highlighted for each zone in the upper bottom corner, the lower top corner, and on the lateral wall. And, three locations are highlighted in the upper top corner. Although, as shown in Fig. 9 to 13, the resolved ω_x transportation terms magnitude increase as the rotation number increases, but their contributions remain the same role for each term. Moreover, those highlighted locations of the resolved ω_x transportation term balances also remain in the same zones, as the rotation number increases. Thus, the resolved ω_x transportation term balances in those highlighted locations will be described in subsubsection 4.2.1 and 4.2.2.

Figures 14 to 19 demonstrate the variety of changes of the secondary flows in the non-rotating and rotating ducts, the contour lines of the resolved ω_x transportation terms are overlaid on the contour colour of the resolved ω_x at different friction rotation numbers. In addition, the half duct results are displayed due to the symmetry of the flows. The present results obtained are in good agreement with the results of Gavrilakis [3] and Pallares and Davidson [7], as mentioned in subsection 4.1. Moreover, the resolved ω_x transportation terms are plotted at specific highlighted locations over the duct cross-sectional area in Fig. 9 to 13.

4.2.1. Stationary Duct

As illustrated in the previous section, secondary flows in the non-rotating duct has the two counter-rotating secondary flows which distributed in each corner of the duct. This secondary flows' mechanism is mentioned in following subsubsubsection.

4.2.1.1. Pair Counter Rotating Secondary Flows

The pair counter rotating secondary flows is investigated in only the lower bottom corner zone due to symmetry of the flows in following subsubsubsubsection.

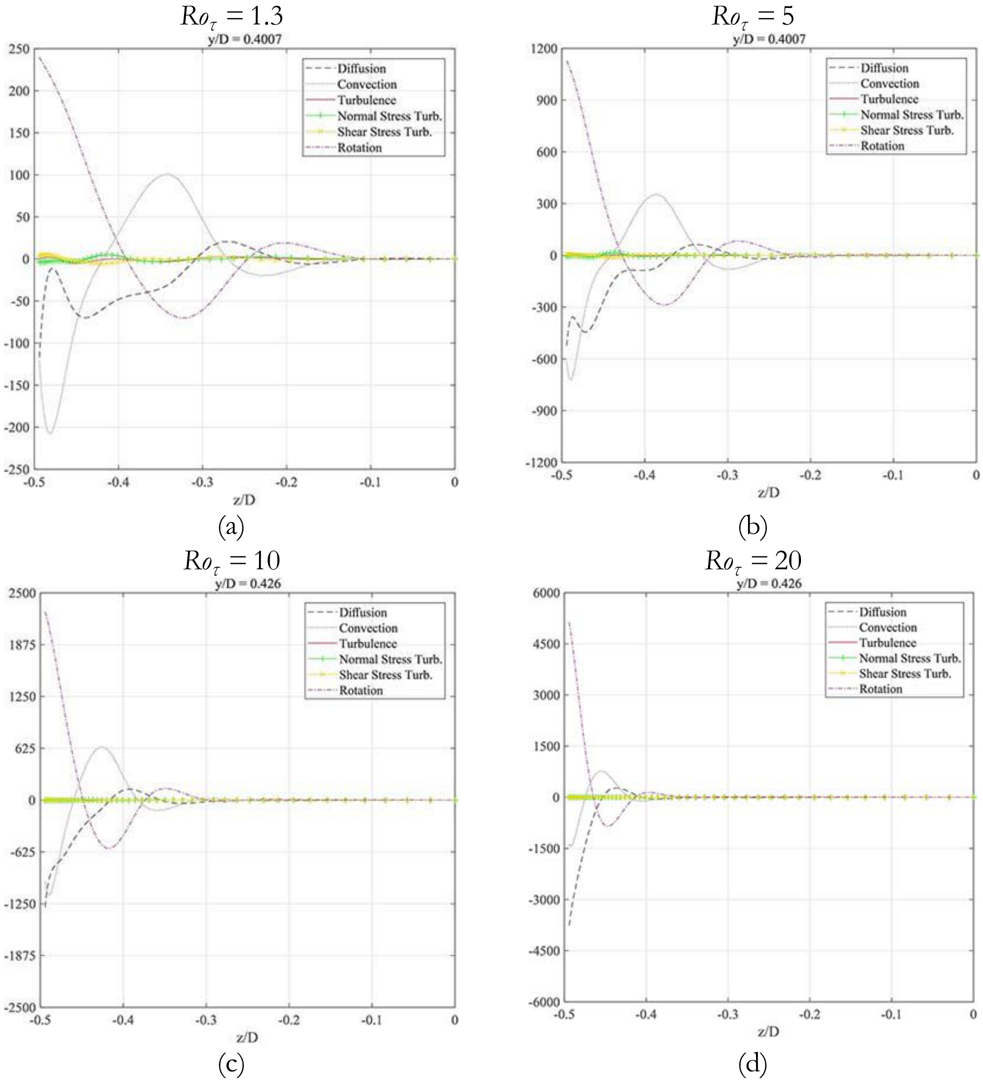

Fig. 13. The resolved ω_x transportation terms at the lower top corner (a) $Ro_\tau = 1.3$; (b) $Ro_\tau = 5$; (c) $Ro_\tau = 10$; (d) $Ro_\tau = 20$.

4.2.1.1.1. Lower Bottom Corner

Naturally, the turbulence induced secondary flows occurs in the stationary duct. As shown in Fig. 9(a), diffusion term plays a dominant role which is balanced by turbulence and convection terms in the lower bottom corner. The turbulence term is dominated by normal stress turbulence term. As shown in Fig. 15(a), diffusion term acts as a source term to the positive streamwise vorticity on the bottom wall, to induce vortices on the wall. The term acts as a sink term to the negative streamwise vorticity above the bottom wall to encounter the secondary flows, due to the presence of the duct wall. Figure 16(a) shows that a local minimum turbulence term is located in-between the negative and the positive streamwise vorticity in the duct corner where a rapid distortion was occurred due to the corner effects. Thus, the turbulence term acts as a source term to the negative streamwise vorticity above the bottom wall, as show in Fig. 19(a), where shear stress turbulence term makes a significant role. However, the turbulence term acts as a sink term to the positive streamwise vorticity within the shear layers on the bottom wall where normal stress turbulence term makes a high contribution, as shown in Fig. 18(a). As shown in Fig. 14(a), positive convection term on the negative streamwise vorticity along the secondary flows beside the corner bisector represents the decrement of the negative streamwise vorticity due to the streamwise vortices transport from low to high intense negative streamwise vorticity. Continuously, negative convection term on the negative streamwise vorticity above the bottom wall is presence due to a transportation from high to low intense streamwise vortices along inclined accelerating currents from the duct corner. However, on the bottom wall in Fig. 14(a), the negative convection term represents the decrement of the positive streamwise vorticity due to the streamwise vortices transport from low to high intense positive streamwise vorticity. The accelerating currents on the bottom wall continuously transfer high intense streamwise vortices within the positive streamwise vorticity to low intense streamwise vortices near the

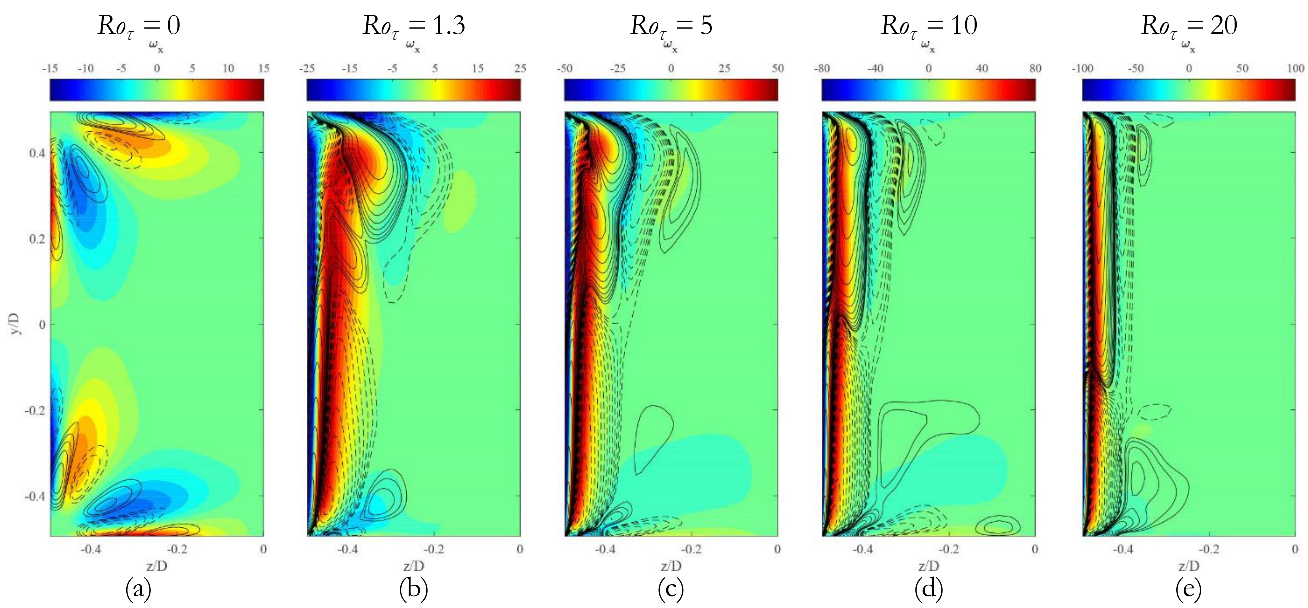

Fig. 14. The resolved ω_x contour colour overlaid with the resolved ω_x convection term contour lines, solid and dash lines for positive and negative values, respectively. The values of the contour lines are the minimum values of -5 and 5 with the 1.4 multiplication decrement and increment, respectively, in every step of the intervals (e.g. ..., -7, -5, 0, 5, 7, ...).

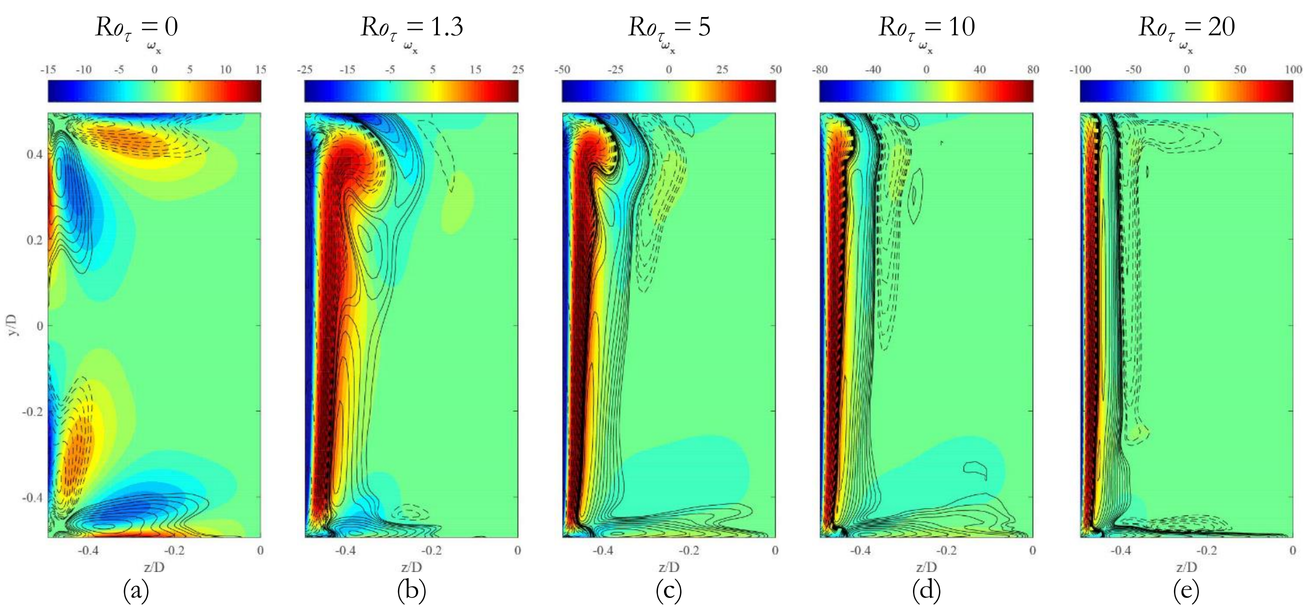

Fig. 15. The resolved ω_x contour colour overlaid with the resolved ω_x diffusion term contour lines, solid and dash lines for positive and negative values, respectively. The values of the contour lines are the minimum values of -5 and 5 with the 1.4 multiplication decrement and increment, respectively, in every step of the intervals (e.g. ..., -7, -5, 0, 5, 7, ...).

bottom wall bisector. Thus, positive convection term is presence at this location.

4.2.2. Rotating Duct

As the duct is rotated, the secondary flows are changed apparently, as illustrated by the streamlines in the Fig. 4. Two large secondary flows with two small secondary flows on the unstable wall are presence in the rotating duct. Both large and small secondary flows' mechanisms are unveiled in following subsubsubsection.

4.2.2.1. Large Secondary Flows

As shown in the Fig. 4 and 8(a), the large secondary flows take up four zones of space over the duct cross

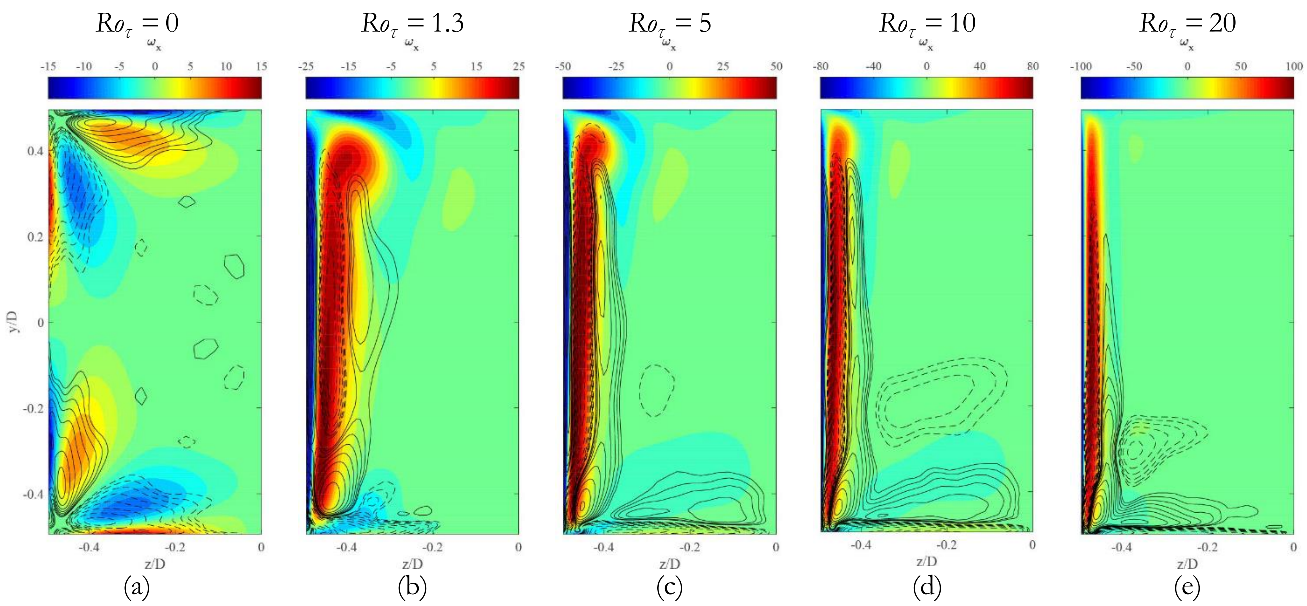

Fig. 16. The resolved ω_x contour colour overlaid with the resolved ω_x turbulence term contour lines, solid and dash lines for positive and negative values, respectively. The values of the contour lines are the minimum values of -5 and 5 with the 1.4 multiplication decrement and increment, respectively, in every step of the intervals (e.g. ..., -7, -5, 0, 5, 7, ...).

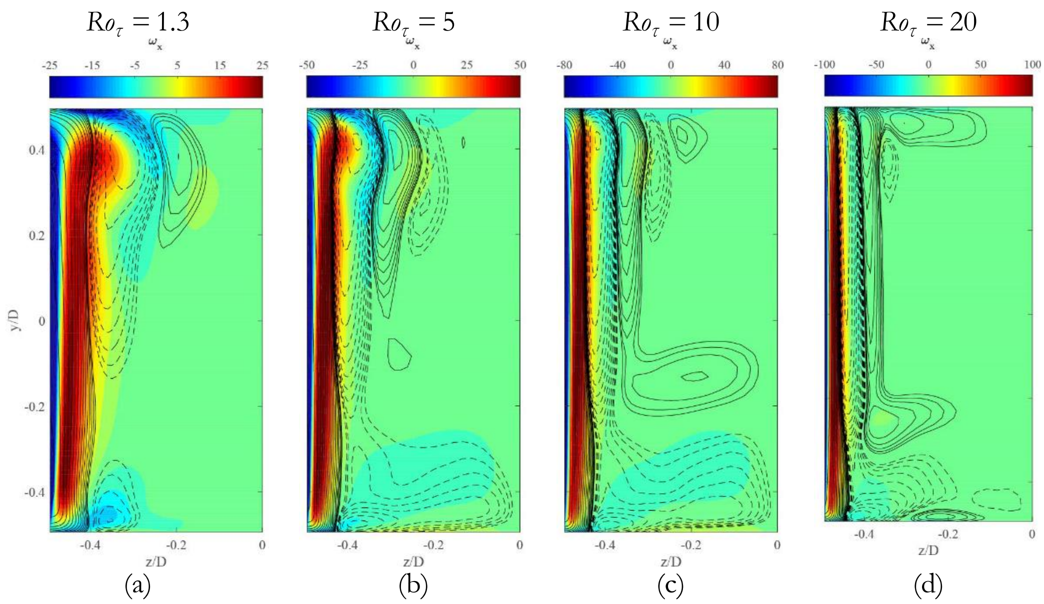

Fig. 17. The resolved ω_x contour colour overlaid with the resolved ω_x rotation term contour lines, solid and dash lines for positive and negative values, respectively. The values of the contour lines are the minimum values of -5 and 5 with the 1.4 multiplication decrement and increment, respectively, in every step of the intervals (e.g. ..., -7, -5, 0, 5, 7, ...).

sectional area. The lateral wall, upper top corner, upper bottom corner, and lower top corner zones are highlighted to evaluated the large secondary flows in following subsubsubsubsection.

4.2.2.1.1. Lateral Wall

Figures 10(a) to 10(d) show that diffusion term plays a dominant role on the lateral wall. The diffusion term is mainly balanced by rotation and convection terms. Moreover, as shown in Fig. 17(a) to 17(d), alternative positive and negative contribution of rotation term represent rotation effects which tend to drive the turbulent flows to be neutralized into the directional preference along the rotational axis. Thus, as shown in

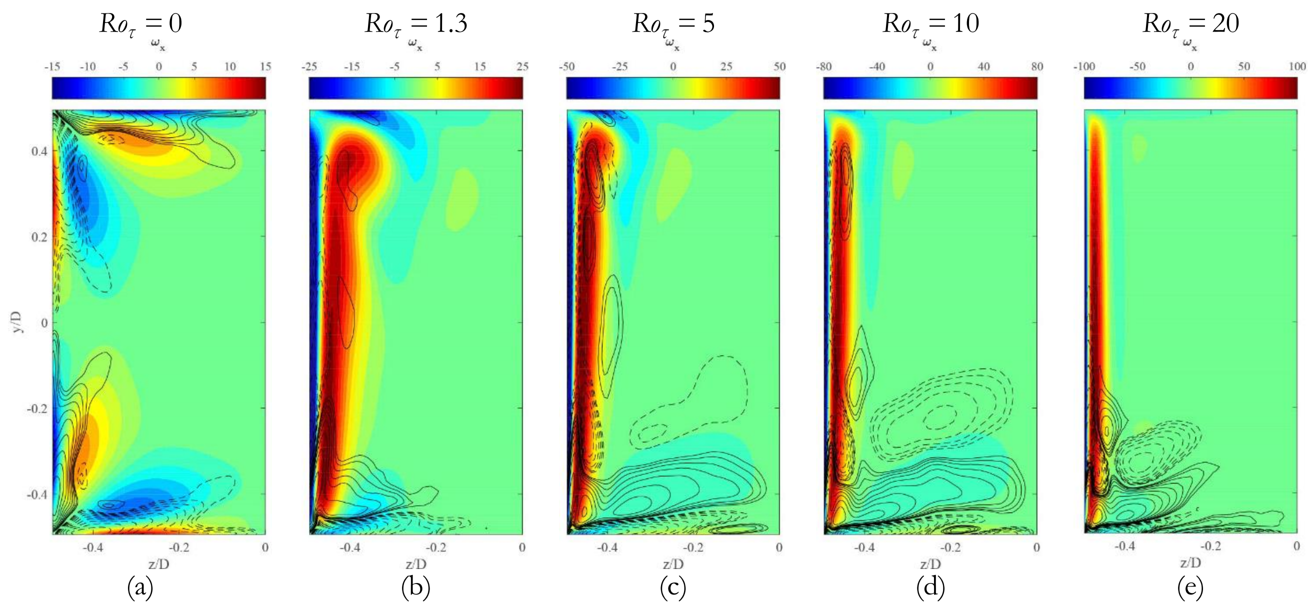

Fig. 18. The resolved ω_x contour colour overlaid with the resolved ω_x normal stress turbulence term contour lines, solid and dash lines for positive and negative values, respectively. The values of the contour lines are the minimum values of -5 and 5 with the 1.4 multiplication decrement and increment, respectively, in every step of the intervals (e.g. ..., -7, -5, 0, 5, 7, ...).

Fig. 15(b) to 15(e), the diffusion term acts as a source term to the negative streamwise vorticity within the Ekman layers on the lateral wall, where the viscous flows is located. As shown in Fig. 14(b) to 14(e), the positive convection term on the negative streamwise vorticity, within shear layer on the lateral wall, represents vorticity transportation from low to high intense streamwise vortices on the wall. On the lateral wall, negative convection term is placed on the negative streamwise vorticity which represents the streamwise vorticity transportation from high to low intense streamwise vortices along the ascending currents of the secondary flows, respectively, from the shear layers on the lateral wall to the top corner.

4.2.2.1.2. Upper Top Corner

As shown in Fig. 11(a) to 11(d), convection and diffusion terms are mainly balanced by each other on the upper top corner. In the upper top corner, as shown in Fig. 14(b) to 14(e), the large secondary flows are circulated out of the top corner. Thus, convection term results as positive on the negative streamwise vorticity at the top wall. This contribution of the convection term represents streamwise vortices transportation from low to high intense streamwise vortices on the wall. The large secondary flows continuously drag high intense streamwise vortices, above the top wall, downward to low intense streamwise vortices. Thus, the convection term results as positive on the positive streamwsie vorticity. In Fig. 14(b) to 14(e), negative convection term on negative streamwise vorticity on the top wall represents vorticity transportation from high intense streamwise vortices on the top wall to low intense streamwise vortices in the duct central region by the large secondary flows circulation. However, as shown in Fig. 15(b) to 15(e), diffusion term acts as sink term to the negative streamwise vorticity along the descending currents within the shear layers on the top wall, in order to expense vortices back to the top wall.

4.2.2.1.3. Upper Bottom Corner

As shown in Fig. 12(a) to 12(d), negative convection term plays a dominant role to positive streamwise vorticity within the upper bottom corner. The convection term is mainly balanced by rotation term at this location. However, as shown in Fig. 16(b) to 16(e), the local maximum turbulence term acts as source term to the positive streamwise vorticity. The local maximum turbulence term is contributed by both normal and shear stress turbulence terms, as shown in Fig. 18(b) to 18(e) and 19(b) to 19(e). In Fig. 14(b) to 14(e), on the upper bottom corner, negative convection term on the positive streamwise vorticity represents vorticity transportation from low intense streamwise vortices in the duct central region to high intense streamwise vortices in the duct corner along descending currents of the large secondary flows. The descending currents are turned upward to the top wall due to the presence of the lateral wall. Then, this ascending currents convect high intense streamwise vortices in the duct corner to low intense streamwise vortices above the lateral wall. Therefore, positive convection term is presence on the positive streamwise vorticity at this location, as shown in Fig. 14(b) to 14(e).

DOI:10.4186/ej.2024.28.5.53

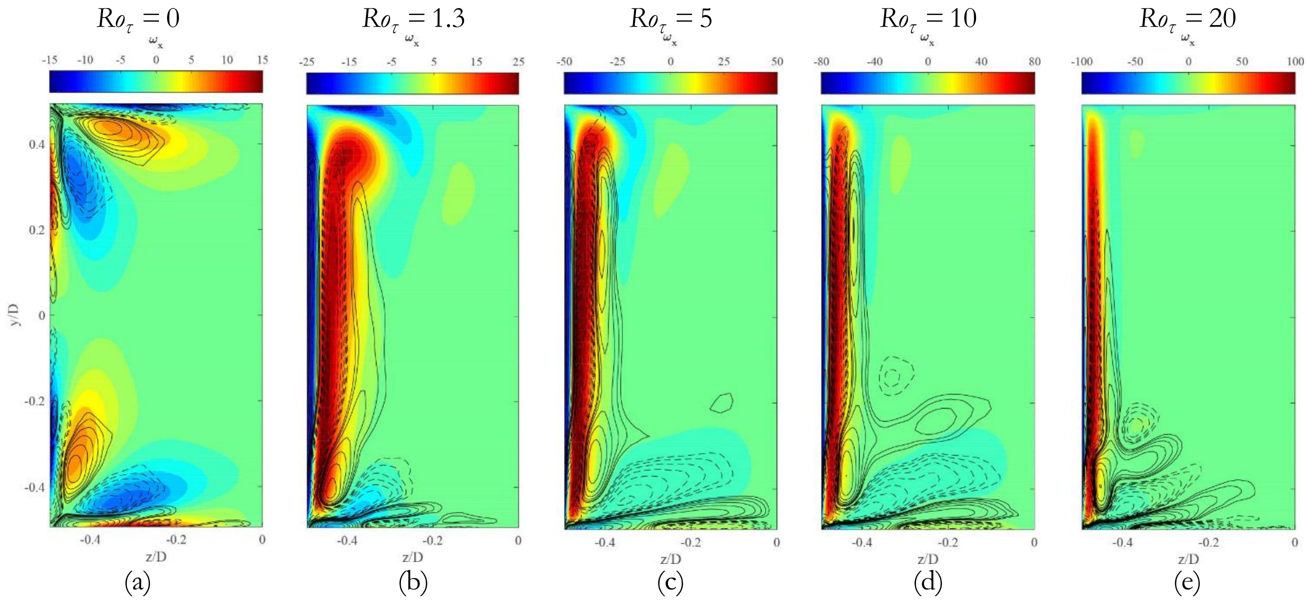

Fig. 19. The resolved ω_x contour colour overlaid with the resolved ω_x shear stress turbulence term contour lines, solid and dash lines for positive and negative values, respectively. The values of the contour lines are the minimum values of -5 and 5 with the 1.4 multiplication decrement and increment, respectively, in every step of the intervals (e.g. ..., -7, -5, 0, 5, 7, ...).

4.2.2.1.4. Lower Top Corner

In the lower top corner, as shown in Fig. 13(a) to 13(d), convection and rotation terms are balanced by each other, where turbulence term is absent and diffusion term has slightly influence at this location. As shown in Fig. 14(b) to 14(e), negative convection term on negative streamwise vorticity represents vorticity transportation from high to low intense streamwise vortices in the lower top corner. However, as shown in Fig. 17(a) to 17(d), rotation term acts as sink term to this negative streamwise vorticity. In addition, diffusion term above the lateral wall acts as sink term to positive streamwise vorticity, in order to dispose vortices to the wall, but rotation term acts as source to the positive streamwise vorticity.

4.2.2.2. Small Secondary Flows

As long as the rotation number increases, the small secondary flows on the unstable wall are behaved visible and barely visible, but persistently be existed as demonstrated by the terms in the streamwise vorticity transport equation. The small secondary flows' mechanism is mentioned in following subsubsubsubsection where the lower bottom corner is the address of the flows.

4.2.2.2.1. Lower Bottom Corner

As shown in Fig. 9(b) to 9(e), diffusion term plays a dominant role as sink term to negative streamwise vorticity on the lower bottom corner, where the local minimum turbulence term is located. The diffusion term is mainly balanced by turbulence and rotation terms at this location. In Fig. 15(b) to 15(e), the diffusion term acts as source term to positive streamwise vorticity on the bottom wall. However, the diffusion term acts as sink term to the negative streamwise vorticity above the bottom wall to regulate the shape of the small secondary flows. A local minimum turbulence term is observed at the reattachment point of the small secondary flow on the unstable wall. The local minimum turbulence term acts as a source term to the negative streamwise vorticity above the bottom wall, as shown in Fig. 16(b) to 16(e). On the bottom wall, as shown in Fig. 17(a) to 17(d), rotation term acts as source term to the negative streamwise vorticity. In addition, consistent contribution ratio between turbulence to rotation terms occur at this location, as the friction rotation number increases from 5 up to 20. As shown in Fig. 14(b) to 14(e), the small secondary flows convect low intense streamwise vortices in the duct central region to high intense streamwise vortices in the lower bottom corner. Thus, positive convection term is presence on the negative streamwise vorticity as the vorticity transportation result. Furthermore, negative convection term on the negative streamwise vorticity represents vorticity transportation due to the accelerating currents convect high intense streamwise vortices in the duct corner to low intense streamwise vortices above the bottom wall. The accelerating currents continuously drag the low intense positive streamwise vortices to high intense positive streamwise vortices within shear layers on the bottom wall. Thus, negative convection term on the positive streamwise vorticity is displayed in Fig. 14(b) to 14(e).

The vortices within the shear layers are continuously transferred along the bottom wall by the accelerating currents which about to detach from the wall to the bottom wall bisector. Thus, high intense streamwise vortices are convected to low intense streamwise vortices within the shear layers on the bottom wall. Therefore, as shown in Fig. 14(b) to 14(e), positive convection term on the positive streamwise vorticity is presence.

5. Conclusion

In this paper, the sequence of the secondary flows in the straight square duct under the effects of rotation is investigated by using the Large Eddy Simulation (LES) with the dynamic kinetic energy subgrid scale model proposed by Kim and Menon [13]. The incompressible fully developed turbulent flows through the duct at the fixed friction Reynolds number of 300 with various spanwise friction rotation numbers of 0, 1.3, 5, 10, and 20 are considered. Thus, this paper studies the turbulent flow mechanisms using the mean streamwise vorticity transport by extended the friction rotation number further from Pallares and Davidson [7].

The obtained results agree qualitatively well with the references. For instance, the present results give the decreasing trend of the bulk Reynolds number as the rotation number increases. Moreover, as the rotation number increases, the eight secondary flows of the turbulence induced secondary flows in the stationary duct are transformed to be the two large secondary flows with the growth and release of the two small secondary flows on the unstable wall. Meanwhile, the Taylor-Proudman region is evident in the central region of the rotating duct. The Ekman layers are placed on the lateral walls.

Investigation into the flow mechanism changes of the secondary flows under the effect of rotation using the transport equation of the resolved mean streamwise vorticity, ω_x, reveals that although the magnitude of the resolved ω_x transportation terms is increased as the duct is rotated, but the contribution of each term remain in the same role. The significant contribution ratio between the turbulence and rotation terms is observed, especially, at the reattachment point of the small secondary flow cell on the unstable wall under the rotation effects. At the reattachment point, both the turbulence and rotation terms of the resolved ω_x transport equation act as the source term to the negative resolved ω_x with the increasing contribution as the rotation number increases. Remarkably, the persistent contribution ratio between the rotation and turbulence terms are found at the reattachment point, as the friction rotation number increases from 5 up to 20, even though the diffusive term plays the dominant role at the position. Meanwhile, curious streamwise vorticity terms have the reciprocal contribution to the secondary flows over the duct cross-sectional area, as the duct is rotated. For instance, the convection and rotation terms are mainly balanced by each other in both the upper bottom corner and the lower top corner. Similarly, on the lateral wall, the diffusion and rotation terms exchanges their contributions to each other. Further than that, the convection and diffusion terms are mainly balanced by each other in the upper top corner. Other than that, as the presence of the Taylor-Proudman region in the duct central region, the rotation term tends to drive the turbulent flows to be neutralized into the directional preference along the rotational axis.

Acknowledgement

Deepest thanks to the Faculty of Engineering, Kasetsart University, Bangkok, Thailand, who gives the graduate research assistant. Further acknowledgement would be done for the Wata Cluster high performance computer where the simulations were performed.

References

[1] A. Huser and S. Biringen, "Direct numerical simulation of turbulent flow in a square duct," *Journal of Fluid Mechanics*, vol. 257, pp. 65-95, 1993.

[2] H. Zhang, F. X. Trias, A. Gorobets, Y. Tan, and A. Oliva, "Direct numerical simulation of a fully developed turbulent square duct flow up to $Re_\tau=1200$," *Abbrev. International Journal of Heat and Fluid Flow*, vol. 54, pp. 258-267, 2015.

[3] S. Gavrilakis, "Numerical simulation of low-reynolds-number turbulent flow through a straight square duct," *Journal of Fluid Mechanics* vol. 244, pp. 101-129, 1992.

[4] R. Vinuesa, A. Noorani, A. Lozano-Duran, G. Khoury, P. Schlatter, P. Fischer, and H. Nagib, "Aspect ratio effects in turbulent duct flows studied through direct numerical simulation," *Journal of Turbulence*, vol. 15, pp. 677-706, 2014.

[5] C. G. Speziale, "On turbulent secondary flows in pipes of noncircular cross-section," *International Journal of Engineering Science*, vol. 20, pp. 863-872, 1982.

[6] F. B. Gessner, "The origin of secondary flow in turbulent flow along a corner," *Journal of Fluid Mechanics*, vol. 58, pp. 1-25, 1973.

[7] J. Pallares, and L. Davidson, "Large-eddy simulations of turbulent flow in a rotating square duct," *Physics of Fluids*, vol. 12, pp. 2878-2894, 2000.

[8] J. Pallares, and L. Davidson, "Large-eddy simulations of turbulent heat transfer in stationary and rotating square ducts," *Physics of Fluids*, vol. 14, pp. 2804-2816, 2002.

[9] J. Pallares, F. X. Grau, and L. Davidson, "Pressure drop and heat transfer rates in forced convection rotating square duct flows at high rotation rates," *Physics of Fluids*, vol. 17, 2005.

[10] Y. J. Dai, W. X. Huang, C. X. Xu, and G. X. Cui, "Direct numerical simulation of turbulent flows in rotating square duct," *Physics of Fluids*, vol. 27, 2015.

[11] X. Fang, Z. Yang, B. C. Wang, and D. J. Bergstrom, "Direct numerical simulation of turbulent flow in a spanwise rotating square duct at high rotation numbers," *International Journal of Heat and Fluid Flow*, vol. 63, pp. 88-98, 2017.
[12] X. Fang, and B. C. Wang, "On the turbulent heat transfer in a square duct subjected to spanwise system rotation," *International Journal of Heat and Fluid Flow*, vol. 71, pp. 220-230, 2018.
[13] W. W. Kim, and S. Menon, "Application of the localized dynamic subgrid-scale model to turbulent wall-bounded flows," in *Aerospace Sciences Meeting & Exhibit*, Reno, 1997.
[14] S. E. Kim, "Large eddy simulation using an unstructured mesh based finite-volume solver," in *AIAA Fluid Dynamics Conference and Exhibit*, Portland, Oregon, 2004.
[15] N. Kharoua, and L. Khezzar, "Large eddy simulation study of turbulent flow around smooth and rough domes," *Proceedings of the Institution of Mechanical Engineers, Part C: Journal of Mechanical Engineering Science*, vol. 227, pp. 2686-2700, 2013.
[16] ANSYS, "ANSYS Fluent Theory Guide release 18.0," ANSYS Inc., Southpointe, 275 Technology Drive, Canonsburg, PA 15317, 2017.
[17] C. W. Huang, V. Srikanth, and A. V. Kuznetsov, "The evolution of turbulent micro-vortices and their effect on convection heat transfer in porous media," *Journal of Fluid Mechanics*, vol. 942, 2022.
[18] W. Sudjai, V. Juntasaro, and V. Juttijudata, "Large eddy simulation of turbulence induced secondary flows in stationary and rotating straight square ducts," *IOP Conference Series: Materials Science and Engineering*, vol. 297, 2018.
[19] M. Breuer, and W. Rodi, "Large-eddy simulation of turbulent flow through a straight square duct and a 180° bend," in *Direct and Large-Eddy Simulation I*, Springer Netherlands, 1994, pp. 273–285.
[20] L. D. Ma, Z. Y. Li, and W. Q. Tao, "Large eddy simulation of turbulent flow and heat transfer in a square duct with unstable natural convection on the cross section," *International Journal of Heat and Mass Transfer*, vol. 66, pp. 46-63, 2013.
[21] J. Yao, Y. Zhao, and M. Fairweather, "Numerical simulation of turbulent flow through a straight square duct," *Applied Thermal Engineering*, vol. 91, pp. 800-811, 2015.

Wisit Sudjai received Master of Engineering and Bachelor of Engineering degrees from mechanical engineering department in Kasetsart University, Thailand. He achieved the best paper award in computation and simulation techniques in the 8th Thai Society of Mechanical Engineers, International Conference on Mechanical Engineering, 2017 (TSME-ICoME 2017) held on 12 to 15 December 2017 at Bangkok, Thailand.

Varangrat Juntasaro received Doctor of Philosophy and Bachelor of Engineering degrees in mechanical engineering from Imperial College London, U.K., in 1999 and 1995 respectively, with the Royal Thai Government Scholarship. She has started working as a lecturer, in 1999, and became Associate Professor, in 2006, and Assistant Professor, in 2001, at Department of Mechanical Engineering, Faculty of Engineering, Kasetsart University, Bangkok, Thailand. Area of her research of interests are computational fluid dynamics (CFD), turbulence modelling, and turbomachinery flow in power plants.

Vejapong Juttijudata received Doctor of Philosophy degree in aerospace engineering from Cornell University, U.S.A., in 2003, with the Royal Thai Government Scholarship. He was appointed as a postdoctoral research associate in School of Mechanical and Aerospace Engineering, Princeton University, in 2004. He has started working as a lecturer, in 2005, and became Associate Professor, and Assistant Professor, at Department of Aerospace Engineering, Faculty of Engineering, Kasetsart University, Bangkok, Thailand. Area of his research of interests are aerodynamics, fluid dynamics and flow control.